

Simultaneous Detection, Demodulation, and Angle-of-Arrival Determination of Communication Signals Using a Dual Ladder Rydberg Receiver

Stone B. Oliver,^{1,2,*} Samuel Berweger,¹ Eugeny E. Mikhailov,³ Dixith Manchaiah,^{1,2} Nikunj Kumar Prajapati,¹ Christopher L. Holloway,¹ and Matthew T. Simons^{1,†}

¹*National Institute of Standards and Technology, Boulder, Colorado 80305, USA*

²*Department of Physics, University of Colorado, Boulder, Colorado 80309, USA*

³*College of William & Mary, Williamsburg, Virginia 23187, USA*

In a typical Rydberg mixer, modulated communication signals are detected using a radio frequency (RF) heterodyne technique. The mixer outputs an intermediate frequency (IF), which must be filtered and mixed down to baseband. In this work, we apply an RF-homodyne technique to demonstrate simultaneous detection and a direct, baseband readout of the in-phase (I) and quadrature (Q) components of standard communication signals using a dual ladder Rydberg receiver. We further show that the inherent polarization sensitivity of this receiver can be used to determine the signal's angle of arrival. We also compare the dual ladder system with a typical Rydberg mixer. The RF-heterodyne-based system's maximum detectable symbol rate is constrained by a signal amplitude which decays with the heterodyne field's detuning from the Rydberg-Rydberg atomic transition used to detect the signal, but the dual ladder design is not subject to this limitation. However, the dual ladder system is more sensitive to low-frequency noise. As a result, its performance is degraded relative to its conventional counterpart when subjected to pink noise. We show that once pink noise effects have been accounted for, both systems behave comparably.

I. INTRODUCTION

Rydberg receivers are Rydberg atom-based sensors designed to detect radio frequency (RF) signals [1–3] which offer several key advantages over traditional RF receivers [4–14]. Traditional RF receivers are size-limited due to 1.) their use of complicated circuits, amplifiers, mixers, and digitizers, and 2.) the fact that the antenna used to receive the signal must have a size comparable to the wavelength of the signal. On the other hand, a Rydberg receiver forgoes much of this complicated hardware, and its physical size is not sensitive to the signal's wavelength. Given their reliance on the fixed, discrete energy structure of atoms, Rydberg receivers can also be self-calibrated. Additionally, traditional RF receivers are band-limited, whereas a single Rydberg receiver could plausibly span a frequency range from ≈ 100 MHz to 1 THz.

A Rydberg mixer [15], also known as an atomic super-heterodyne receiver [16], is a phase-sensitive Rydberg receiver capable of detecting standard communication signals (e.g., amplitude phase shift keying (APSK), 16 quadrature amplitude modulation (16QAM), etc.). It is comprised of a two-photon electromagnetically induced transparency (EIT) spectroscopy system and an RF field tuned to a Rydberg-Rydberg atomic transition. In this situation, the RF field produces Autler-Townes (AT) splitting in the EIT feature. Using the RF field as a local oscillator (LO), the Rydberg receiver acts as a free-space mixer which down-converts an incoming RF signal to an intermediate frequency (IF). The IF is then encoded in the EIT signal. Using a spectral filter to remove negative frequency components and mixing the recorded IF down to baseband, the in-phase (I) and quadrature (Q) components of the signal correspond to the real and imaginary parts of the output, respectively. Given its prevalence in the literature, we refer to this receiver design as a conventional Rydberg receiver (CRR).

* stone.oliver@nist.gov

† matt.simons@nist.gov

While a CRR typically relies on the use of RF-heterodyne detection, one can also use RF-homodyne detection, where the LO frequency is matched to the signal frequency. Applying RF-homodyne detection to a CRR, any modulation encoded in the signal is directly converted to baseband, but the output is insensitive to any components of the signal which are out of phase with the LO. For this work, we use 'out of phase' to refer exclusively to two waves being 90° out of phase with respect to one another. Thus, a CRR can be used in conjunction with RF-homodyne detection to receive amplitude modulated signals which are not out of phase with the LO [17], but it will be generally ineffective in detecting phase modulated signals (i.e., it can measure either I or Q, but not both).

This limitation can be circumvented through the simultaneous use of two independent, spatially overlapped CRRs, where the LO fields of each CRR are out of phase with one another. We refer to this design as a dual ladder Rydberg receiver (DLRR) [18], and we refer to the individual receivers therein as the arms of the DLRR. In this situation, a signal which is out of phase with one arm will be in phase with the other, and vice-versa. As such, one can use RF-homodyne detection with the DLRR to directly measure I with one arm and Q with the other, removing the need to filter out negative frequency components and mix the signal down to baseband. Hence, the DLRR simultaneously detects and demodulates amplitude and phase modulated signals. As with a CRR, the DLRR is also sensitive to the signal's relative phase.

Another advantage of the DLRR is its inherent ability to determine a signal's angle of arrival (AoA) through a single measurement at a single spatial location [19]. As the DLRR relies on setting the RF-polarization of each arm's LO orthogonal to the other, the magnitude of the signal recorded by each arm varies based upon the signal's polarization overlap with each LO. The ratio of the signal amplitude recorded by each arm can then be used to determine the signal's AoA.

The maximum detectable symbol rate for each system is also influenced by different fac-

tors (the symbol rate is defined as the rate at which the signal is altered by the applied modulation, corresponding to the number of symbols transmitted per second). Within any AT-splitting based Rydberg-atom receiver, the signal amplitude is maximal when the signal frequency equals the Rydberg-Rydberg transition frequency in the atoms [20, 21]. Assuming the signal is set to this ideal frequency, the DLRR will then exhibit a maximal amplitude, regardless of the signal's symbol rate. On the other hand, a CRR necessitates the use of an IF, and thus fails to function when either the LO or the signal are detuned such that the amplitude falls below the noise floor of the system. Since the IF must be approximately greater than or equal to the signal's symbol rate, the AT-splitting amplitude contributes to the upper limit on the CRR's maximum detectable symbol rate. While the DLRR is not subject to this limitation, it is more sensitive to low frequency noise.

In this article, we demonstrate the simultaneous detection and direct, baseband readout of the I and Q components of standard communication signals using the DLRR. We also demonstrate the system's ability to resolve the signal's relative phase and AoA. Finally, the system's performance is compared with a CRR, and the influence of the frequency distribution of noise within each system is discussed.

II. EXPERIMENTAL SETUP

A. Constructing the Dual Ladder Rydberg Receiver

We construct the DLRR according to the process outlined in [18]. In order to achieve two spatially overlapped, yet independent CRRs, we begin with two standard, two-photon ladder-type EIT systems [22, 23] which utilize orthogonal optical polarizations and frequencies which are detuned from one another. These choices result in each system interacting with different Doppler classes of atoms, and orthogonal polarizations, thereby eliminating cross-talk between them. The first EIT system is built using a

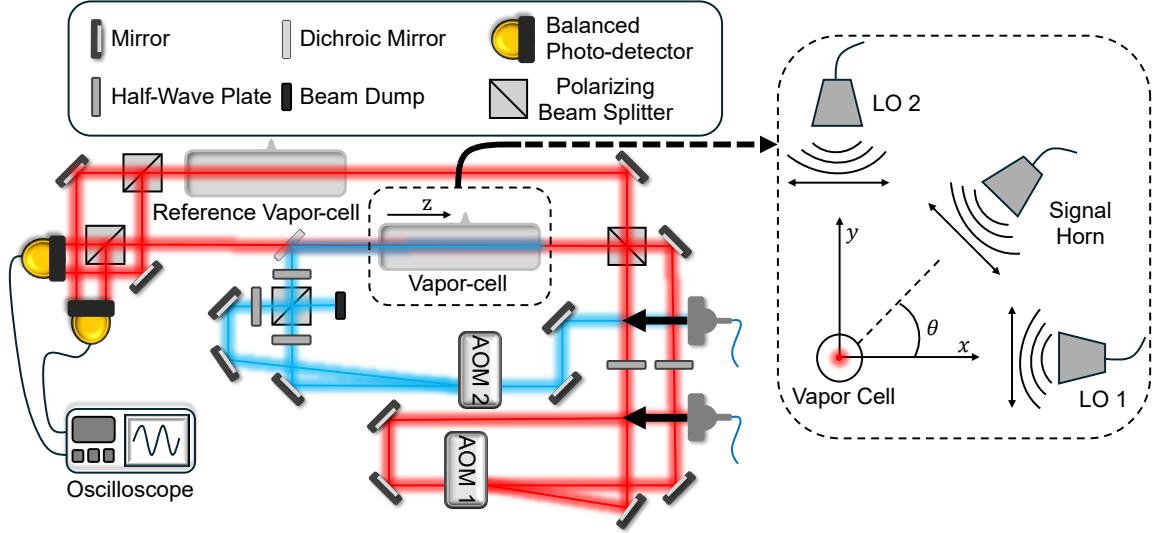


FIG. 1. Schematic of the optical setup and the orientation of the RF horn-antennas relative to the vapor cell. The black arrows out of the fiber couplers indicate the direction of laser propagation. Red laser beam paths indicate 780 nm light, while blue paths indicate 480 nm light. The angle θ describes the relative angle between LO 1 and the signal horn, i.e., the AoA. The z-direction is taken to be opposite the direction of the probe's propagation at the vapor-cell.

780 nm probe laser tuned to the $D2$ transition of 85-Rubidium and a 480 nm pump laser tuned to couple the $D2$ state to the $54D_{5/2}$ state. Prior to entering a glass vapor cell containing room-temperature Rubidium atoms, both beams are linearly polarized along the same axis. Additionally, the beams are directed into the cell from opposite directions in order to partially cancel Doppler broadening effects. EIT is observed by scanning the pump laser frequency and measuring the probe transmission through the vapor cell. Figure (1) provides a schematic of the experimental setup, while figure (2) depicts the energy level diagram for the EIT setups.

In order to construct the second system, the pump and probe lasers are passed through acousto-optic modulators (AOMs) such that the probe laser is red-shifted by $-c/\Delta_1 \approx -80$ MHz while the pump laser is blue-shifted by $+c/\Delta_2 \approx +130$ MHz where c is the speed of light and Δ_i refers to the wavelength shifts shown in figure 2 (the original EIT setup is constructed us-

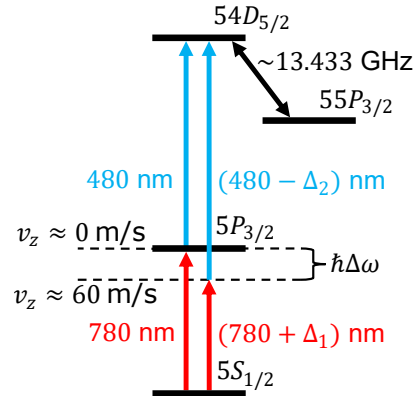


FIG. 2. Above shows the energy level diagram for 85-Rubidium used to construct the DLRR. To achieve independent sensing, the second EIT system interacts with the same states as the first, but accesses them through a different Doppler class of atoms. The atom velocity which shifts the beams to resonance is provided on the left, where the positive z-direction is taken to be opposite the direction of the probe's propagation.

ing the 0th order light from each AOM). These frequency-shifted beams are then linearly polarized orthogonally to their original counterparts and recombined with those counterparts in order to produce two spatially overlapped EIT setups. To improve the signal to noise ratio (SNR) in this setup, we employ balanced detection, where the reference beams for each EIT system are also spatially overlapped and sent through a separate, but identical vapor cell. For both EIT systems, the probe laser was set to a power of $\approx 100 \mu\text{W}$ with corresponding Rabi rate $\approx 7 \text{ MHz}$, while the pump laser was set to a power of $\approx 60 \text{ mW}$ with a corresponding Rabi rate of $\approx 2 \text{ MHz}$. Figure (3) shows the EIT spectra acquired by measuring each probe lasers' transmission.

To finish constructing the DLRR, we add to each EIT system an RF horn-antenna tuned to a Rydberg-Rydberg transition in the atoms. The field produced by each horn acts as the LO for its respective arm. For our work, we use the $54D_{5/2}$ to $55P_{3/2}$ transition, which was calculated to be 13.433374 GHz using the Alkali-Rydberg calculator in Python [24]. Three conditions must be met when placing these horns. First, each horn must be placed such that the atoms are in the Fraunhofer region (i.e., the far field region) of the radiation field, meaning the radiation may be treated as a plane-wave with a well-defined polarization. Second, both horns must be oriented such that their polarizations match the polarization of their respective EIT beams. Third, the field produced by one horn-antenna at the vapor cell must be out of phase with the field produced by the other horn (i.e., the LO fields must be out of phase with one another).

B. Generating and Detecting a Signal

To complete the experimental setup, we add a third RF horn-antenna in order to provide the signal which the DLRR will detect and demodulate. As with the LO horn-antennas, it must be placed sufficiently far from the vapor cell. To generate a modulated signal, we

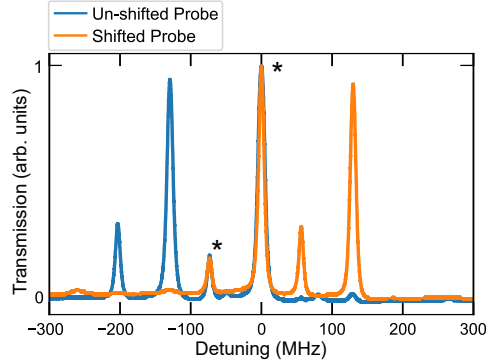


FIG. 3. Above displays the EIT spectra acquired by measuring the transmission profile of each probe beam while scanning the pump beams of the DLRR. Since all four beams are spatially overlapped, each spectrum shows two pairs of EIT features separated by the detuning between the pump beams. The smaller peak seen in each pair corresponds to the $54D_{3/2}$ state, while the larger peak corresponds to the $54D_{5/2}$ state. The difference between these peaks was used to calibrate the frequency axis. The features marked with a * correspond to the frequency-overlapped features, the larger of which was used for this work. The unmarked features result from beam cross-talk and do not impact the experiment.

use an arbitrary waveform generator (AWG) set to output a modulated tone. Using either a 16QAM, APSK, or quadrature phase shift keying (QPSK) modulation scheme, we select the desired symbol rate and generate a pseudo-random (PN) sequence of 511 symbols (i.e., we generate 511 constellation points, where the duration of the transmitted signal is given by 511 divided by the symbol rate). Since the AWG used for this work cannot directly produce modulated signals at 13 GHz , we mix the AWG output with a pure RF-tone using a conventional mixer to produce a modulated signal at the desired frequency. The frequency of the resulting signal is given by

$$f_c + f_p = f_s, \quad (1)$$

where f_c refers to the modulated carrier frequency produced by the AWG, f_p refers to the pure RF-tone, and f_s is the modulated signal

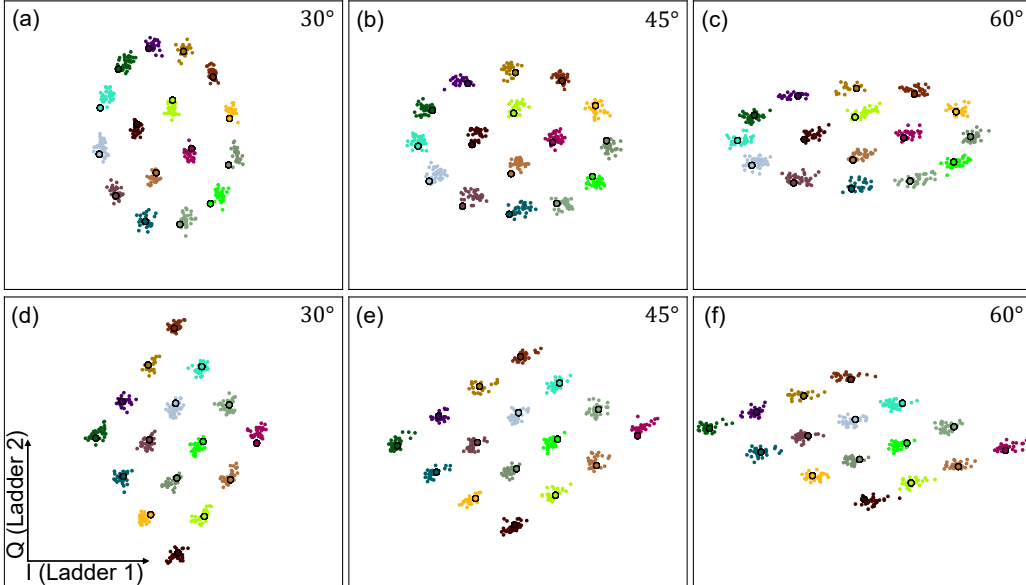


FIG. 4. Above shows three APSK and three 16QAM I/Q diagrams as a function of the received signal’s measured AoA; each constellation is compressed or expanded along each axis according to equation 2. The individual points in each sub-plot are measured data, while each black circle with a distinct color inside represents a nominal constellation point. (a) APSK with AoA = 30°. (b) APSK with AoA = 45°. (c) APSK with AoA = 60°. (d) 16QAM with AoA = 30°. (e) 16QAM with AoA = 45°. (f) 16QAM with AoA = 60°.

frequency. For this work, we set $f_c = 1$ GHz and $f_p = 12.433\,374$ GHz, yielding a modulated signal at frequency $f_s = 13.433\,374$ GHz. The signal is finally sent to and emitted from the signal horn-antenna onto the atoms. The signal is then encoded in the transmission profile of the probe beams, which first pass through the atoms, and then are sent into photo-detectors. The output voltage of these detectors are measured using an oscilloscope.

When the signal field is incident at angle $\theta = 45^\circ$ relative to each LO field, it will interact equally with both arms because it possesses equal polarization components along each axis (see figure (1)). As a result, the relative amplitudes of the measured I and Q values will match their nominal values. As θ deviates from 45° , the polarization overlap of the signal with each arm will vary, resulting in a shift in I and Q

given by

$$\begin{aligned} I(\theta) &= I_0 \sin(\theta) \\ Q(\theta) &= Q_0 \cos(\theta), \end{aligned} \quad (2)$$

where I_0 and Q_0 refer to the nominal values of I and Q for the given transmission (i.e., the values of I and Q expected when $\theta = 45^\circ$). To explicitly depict the way in which the angle of incidence warps the constellation diagram, figure (4) shows three APSK constellation plots and three 16QAM constellation plots collected using signal horn angles $\theta = 30^\circ, 45^\circ$, and 60° . Comparing the ratio I_0/Q_0 with the ratio between the relative signal amplitudes measured along each arm of the receiver, $I(\theta)/Q(\theta)$, one can deduce the signal’s AoA. Note that equation 2 is idealized and does not consider effects such as RF-reflections or imperfect polarization (see appendix A).

C. Analyzing the Detected Signal

In order to analyze a given measurement, we first apply a low-pass spectral brickwall filter to the signals recorded by the oscilloscope to remove all frequency components with a frequency larger than the symbol rate used for that measurement. Note, however, that the DLRR does not strictly require the use of a filter to determine I/Q values, as there is no need to remove negative frequency components as is the case with RF-heterodyne detection. To determine the n^{th} symbol's I/Q position, we then choose to take the measured values of the center point of the symbol's duration.

Once the data is filtered and analyzed, we determine the received signal's relative phase and AoA by comparing to a reference list of nominal I and Q positions for the given PN-sequence and modulation scheme as a function of the signal's phase and AoA. Each list is comprised of $90 \times 360 = 32400$ entries, corresponding to calculations of the nominal I/Q positions in one degree increments over the unit circle for phase and over the range 0° to 90° for AoA. Subtracting each nominal point set from the measured points to produce a set of error functions, the phase and AoA of the nominal point set which produces the error function of minimal magnitude is taken to be the measured signal's phase and AoA. Using the nominal point set, we also calculate error-vector-magnitude (EVM), where the root-mean-square magnitude of the nominal points is used for normalization [25].

For all data related to the signal's AoA and or phase presented in this work, we apply a symbol rate of 10 kBaud. For data related to system comparison with a CRR, the signal horn was placed at an angle of $\theta = 45^\circ$ relative to both LOs. Lastly, note that when using the DLRR to detect these signals, we tune the power applied to both the LOs and the signal in order to optimize the SNR. For this work, each LO was set to an output power of ≈ -16 dBm, while the signal power was ≈ -6 dBm. These powers were fixed as the symbol rate was varied.

Notably, the use of a matched filter is often desirable because it maximizes SNR [26]. A

matched filter allows one to extract I and Q via maximization of the cross-correlation between the expected signal and the received signal. Furthermore, the use of a spectral brickwall filter on a modulated signal comprised of square pulses inherently leads to error because the filter truncates a portion of the signal's frequency distribution. However, this choice is motivated by the fact that a matched filter is an idealized filter for systems that experience primarily additive noise. As will be discussed in the next section, the DLRR is subject to substantial multiplicative noise (i.e., noise which scales with the signal amplitude). The presence of multiplicative noise renders a matched filter less effective; correlating a received, noisy signal with the nominal signal cannot remove noise which also correlates with the nominal signal. As the use of a spectral brickwall filter is equivalent to convolving the received signal with a sinc function, cross-correlation no longer serves as an effective mechanism for determining I and Q. By instead choosing to only select the center point of the symbol's duration, error induced by the brickwall filter is reduced to a scaling error which is corrected by normalizing the data to the mean of its absolute value. Indeed, the accuracy of this approach was found to be substantially better than the accuracy obtained through the use of a matched filter. One other advantage of this analysis method is that the use of a spectral brickwall filter only requires knowledge of the symbol rate, which can be effectively estimated without any prior knowledge of the signal [27–30].

III. RESULTS AND DISCUSSION

A. Determining Angle of Arrival and Relative Phase

The AoA data presented in this section is the result of five separate measurement runs. Two measurements used a 16QAM modulation, two used APSK, and one used QPSK. For each measurement run, we vary the signal horn's position from $\theta = 10^\circ$ to $\theta = 80^\circ$ in 5° increments. At

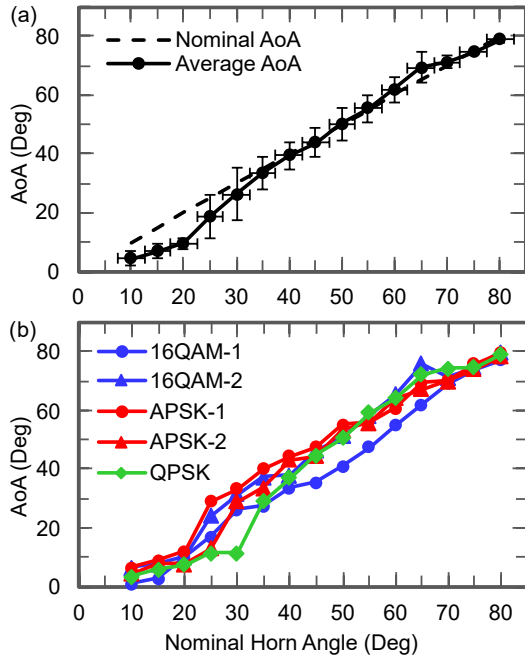


FIG. 5. (a) displays the AoA found by averaging all five measurement runs. Vertical error bars represent one standard deviation, while the horizontal error bars represent absolute limits on the signal horn position. (b) displays the phase-averaged AoA measurement results of each measurement run. The color coding used here to represent different modulation schemes is maintained throughout this work.

each angle, we vary the signal’s relative phase in 30 degree increments around the unit circle, yielding twelve measurements at a given AoA, where each individual measurement therein is an average of 16 traces from an oscilloscope. The oscilloscope was set to collect 12.5 MSa/s. Averaging over the five measurement runs, the EVM was found to be approximately $15 \pm 3\%$.

Figure (5a) shows the average of all five measurement runs. The average measured AoA well-matches the signal horn’s angle for angles above approximately 25° . The reason for deviation at lower horn angles is thought to be a result of cross-talk resulting from RF-reflections off of the vapor cell. This topic is discussed further in appendix A. Figure (5b)

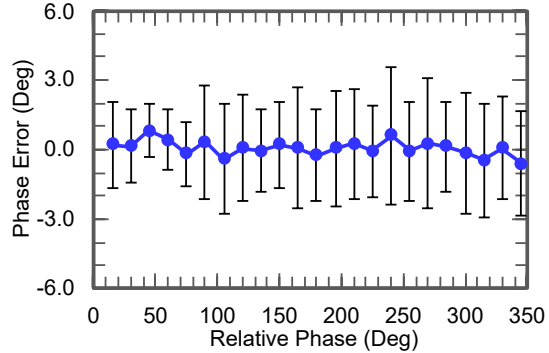


FIG. 6. Above shows the deviation of the measured relative phase of a 16QAM signal from its nominal value, averaged over signal horn angles ranging from 10° - 80° in 5° increments. The error bars represent one standard deviation.

shows the phase-averaged AoA versus the signal horn’s true placement for each measurement run. These results indicate that the AoA measurement is generally independent of the modulation scheme applied. This is also evident from the fact that the standard deviation of the EVM across these modulation schemes was not found to be of notably higher or lower average for one modulation scheme over another.

We also investigate the DLRR’s ability to determine a signal’s relative phase. We apply a 16QAM modulation and take the phase of the first measurement to be zero. We then vary the phase in 15° increments over the unit circle, yielding twenty-four measurements at a given horn angle. As with the AoA data discussed above, we vary the horn-angle over a range of $\theta = 10^\circ$ to $\theta = 80^\circ$, evenly spaced by 5° increments, yielding a total of 344 relative phase measurements (one measurement was removed from the sample). We then determine the AoA-averaged relative phase error, depicted in figure (6). The average relative phase error was found to be approximately $0^\circ \pm 2^\circ$.

B. Comparison of the Direct Conversion Rydberg Receiver with a Conventional Rydberg Receiver

We also compare the DLRR with a CRR. To produce a CRR with comparable characteristics, we turn off LO2 (see figure (1)) and detune the signal frequency f_s in equation 1 from the remaining LO to generate an IF (i.e., a beatnote). This is achieved by detuning f_p . No other characteristics of the system are altered. Since the IF must be approximately equal to or larger than the symbol rate, we set the IF equal to the symbol rate. We then apply a QPSK modulation, and the modulated IF is detected by measuring the un-shifted probe transmission. We also mix the signal down to baseband prior to applying a low-pass spectral brickwall filter.

To compare the DLRR with the CRR, we vary the modulation's symbol rate and determine the EVM of the recorded signal. As the intensity spectrum of a laser is well-known to exhibit $1/f$ [31], we expect the DLRR to exhibit higher EVM owing to the signal's frequency distribution being centered at 0 Hz. Since the measured signal amplitude scales directly with probe intensity, this pink noise is also multiplicative in nature. Indeed, the noise spectrum appears to be dominated by multiplicative pink noise, and the DLRR was found to exhibit a larger total EVM than the CRR for symbol rates higher than approximately 300 kHz (see appendix B). The exact frequency where this deviation occurs depends upon the spectral overlap between noise and signal. This is determined by 1.) the width of the pink noise profile, and 2.) where the signal's frequency spectrum is centered. The CRR reduces this overlap by centering the signal at the IF rather than 0 Hz. However, we expect both systems to behave comparably once pink noise is accounted for. This behavior is displayed in figure (7), which plots EVM versus symbol rate for both systems after the removal of multiplicative noise effects. Both the total EVM (i.e., EVM where multiplicative effects have not been removed) and the process of removing multiplicative noise effects are discussed in appendix B.

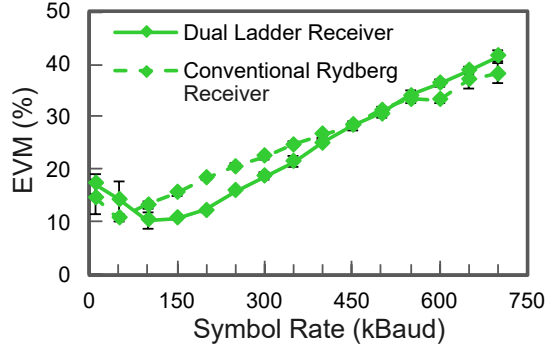


FIG. 7. Above plots signal EVM versus symbol rate for both the DLRR (homodyne) and the CRR (heterodyne), where multiplicative noise effects have been removed. Both measurements used QPSK modulation. For the CRR, the IF was set equal to the symbol rate. Each data point is an average of five measurements. The error bars represent one standard deviation.

IV. CONCLUSION

In this work, we have demonstrated a direct, baseband detection and simultaneous demodulation of the I and Q components of 16QAM, APSK, and QPSK signals through the use of a DLRR which utilizes RF-homodyne detection. In addition to determining a signal's relative phase, we have also shown that this detection scheme allows for a determination of the modulated signal's AoA (a capability which cannot be achieved through a single measurement using a CRR). While the measurement results displayed a monotonic relationship between measured versus nominal AoA, the measured AoA deviates substantially from the nominal value below approximately 25° . This deviation is thought to result from RF-reflections inside the glass vapor-cell used for the experiment which causes cross-talk between each arm of the DLRR, meaning the measurement is sensitive to the exact geometric configuration of the setup (see appendix A).

Additionally, the performance of the DLRR was compared to a CRR through the use of a QPSK signal with varying symbol rates. Mea-

measurements made using the CRR used an IF set equal to the modulation’s symbol rate. After the removal of multiplicative pink noise effects (see appendix B), the DLRR showed comparable EVM to the CRR. However, the total EVM of the DLRR is larger than the total EVM seen in the CRR at higher symbol rates. This indicates that sensor performance is influenced by both the type (additive versus multiplicative) and frequency distribution (pink versus white) of noise present in each system. The substantial quantity of multiplicative pink noise in these systems also justified the use of a low-pass spectral brickwall filter followed by the extraction of I and Q via use of the center point of each symbol’s duration. It remains plausible that a DLRR with minimized noise could outperform its conventional counterpart, owing to the fact that a DLRR does not require the use of an IF, meaning the maximum detectable symbol rate is not limited by the AT-splitting amplitude, which begins to decay when the detuning of incident RF-radiation is on the order of 1 MHz [21].

Future work may include a systematic investigation and reduction of experimental noise to study the interplay between the functionality of each sensor design and noise present in each system or its environment. A substantial reduction in noise would also enable the use of modulation schemes which require lower EVM than the values reported in this work (e.g., 64QAM). The result would be a Rydberg atom-based sensor which not only directly demodulates a signal and determines that signal’s AoA and relative phase, but also detects signals with symbol rates higher than achievable using any currently available Rydberg sensor.

ACKNOWLEDGMENTS

The authors would like to thank Rajavardhan Talashila for valuable simulation results, as well as Daniel Hammerland and Link Patrick for advice and support related to the optical setup. The authors would also like to thank Joshua Kast for valuable conversation related to I/Q

demodulation.

This research was developed with funding from NIST. The views and opinions of authors expressed herein do not necessarily state or reflect those of the United States Government or any agency thereof. A contribution of the U.S. government, this work is not subject to copyright in the United States.

CONFLICT OF INTEREST

The authors have no conflicts to disclose.

DATA AVAILABILITY STATEMENT

All of the data presented in this paper is available at <https://doi.org/10.18434/mds2-4053>

Appendix A: System Diagnostics, Calibration, and Geometric Sensitivity of the DLRR

To verify independent sensing along each arm of the DLRR, we measure each arm’s response to each LO, separately. Following the procedure outlined in reference [18], we turn LO1 on while LO2 and the signal horn are both left off and measure the resulting EIT spectra. We then repeat this process, except we turn on LO2 while LO1 is left off. Since the polarization of each LO and its corresponding EIT system are matched, AT-splitting of the EIT feature occurs in one arm, but not the other. Swapping which LO is on, the AT-splitting moves from one arm to the other. Fitting two Gaussian curves to the split peaks, one can deduce the magnitude of the electric field the atoms experience; the field strength scales linearly with the square root of the power of the LO horn-antenna. This diagnostic offers a straightforward method of measuring the magnitude of unwanted cross-talk between each arm of the receiver. Figure (8) shows the dependence of the probe beams’ transmission spectra as a function of which LO is used and the power of that LO. Given the sensor

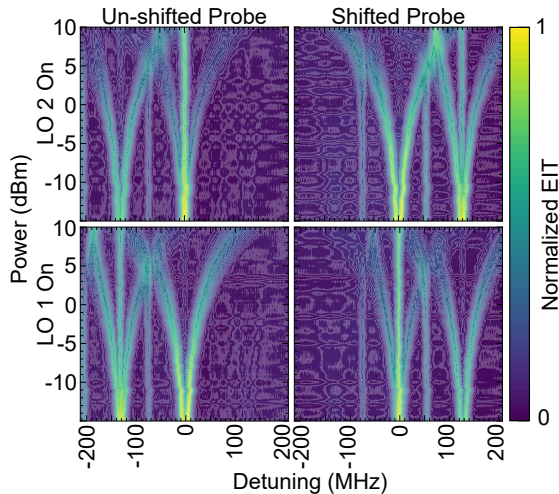


FIG. 8. Above shows waterfall plots of the probes’ transmission amplitudes as a function of both LO power and frequency detuning from the center of the EIT feature. Clearly, one arm’s EIT feature splits in the presence of an applied field from its corresponding LO, while the other arm’s EIT feature still exhibits a distinct peak at zero detuning. The roles reverse upon switching LOs.

must operate with the pump lasers fixed at zero detuning from the overlapped EIT peaks in figure (3), these plots demonstrate independent sensing along each ladder, with sufficiently small cross-talk between them when one LO is left off. However, the system’s performance was found to be dependent upon the exact position of the vapor cell.

While the vapor cell was partially insulated from the environment using RF-absorbing material and raised approximately 50 cm from the table in order to reduce the effects of other reflected fields, cross-talk is still thought to result from RF-fields inside the cell resulting from reflection off of the glass walls of the cell. This hypothesis is supported by the fact that adjusting the vapor cell’s position along the y-direction in figure (1) by ± 2 mm produced a change in the measured of AoA of approximately $\pm 8^\circ$. This sensitivity to physical positioning implies the need for a calibration curve when using the DLRR to determine a signal’s AoA. It also im-

plies that the ideal cell-position which minimizes cross-talk will vary based upon the applied RF-frequency. AoA data was also collected using a QPSK modulation at 17.041 GHz, corresponding to the $50D_{5/2}$ to $51P_{3/2}$ transition. Indeed, the system was found to behave comparably, but only after re-optimization of the vapor cell’s position.

Appendix B: Multiplicative Noise in Rydberg Receivers

Figure (7) displays comparable EVM between the DLRR and CRR only after the removal of multiplicative noise effects. Figure (9a) instead shows the total EVM, without the removal of any noise contributions. The clear difference between these two plots highlights the effect of the multiplicative pink noise discussed in section 9. In this section, we address this discrepancy through an analysis of how the frequency distribution and type of noise each contribute to EVM. Figure (9b) plots EVM which results from multiplicative noise, and figure (9c) is a reproduction of figure (7) for direct comparison. Figure (10) displays the frequency distribution of noise measured by the CRR with no signal present. The noise profile recorded for the DLRR is of functionally identical shape.

In addition to this noise, the atom response time and the amplitude of the AT-splitting feature also contribute to EVM, as the AT-splitting amplitude affects the SNR, and the atom response time can affect the system’s ability to transition between symbols [32]. We refer to these additional effects collectively as atomic noise, as these effects fundamentally result from light-matter interaction inside the cell. We break the EVM into two components; one results from the non-atomic noise profile, the other results from atomic noise. We express this as a function of the symbol rate:

$$\text{EVM} = E_0(S) + E(S), \quad (\text{B1})$$

where $E_0(S)$ refers to atomic noise induced EVM, and $E(S)$ refers to non-atomic noise induced EVM. Since both systems utilized the

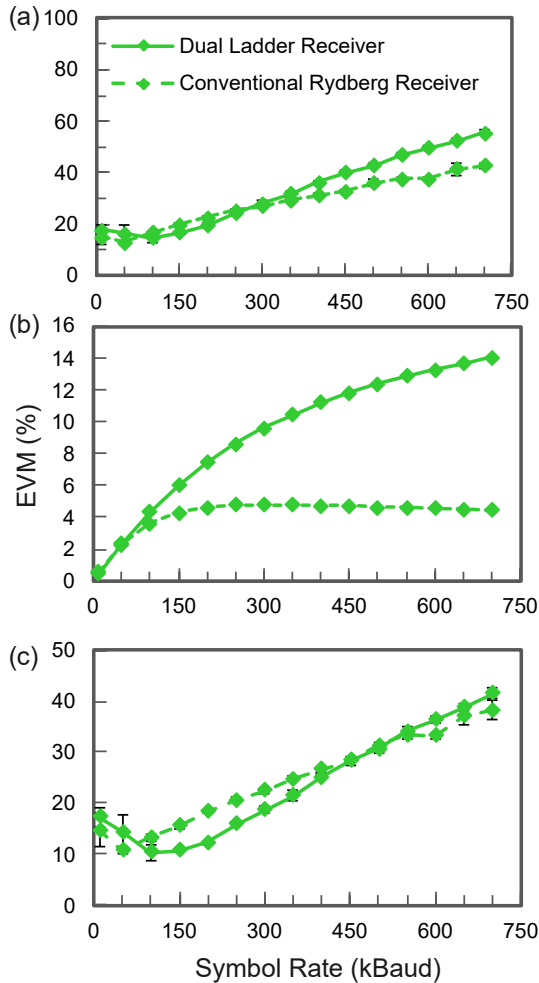


FIG. 9. (a) plots signal total EVM versus symbol rate for both the DLRR (homodyne) and the CRR (heterodyne), where no noise components have been removed. Both measurements used QPSK modulation. For the CRR, the IF was set equal to the symbol rate. Each data point is an average of five measurements. The error bars represent one standard deviation. (b) plots the EVM which results from multiplicative noise effects, such as the probe laser’s $1/f$ noise. (c) plots the residual EVM which results primarily from additive noise. This plot is identical to figure (7).

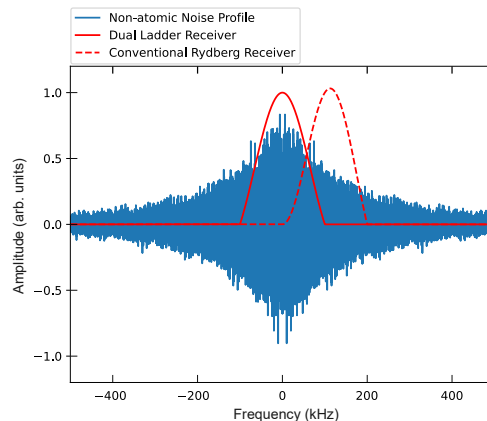


FIG. 10. Above plots the recorded non-atomic noise profile detected by the CRR (blue) and the envelope of the nominal frequency distribution of the received signal expected using either the CRR (dashed red) and the DLRR (solid red) after truncation with a spectral brickwall filter such that only the primary lobe of the envelope remains (compare with equations B3 and B4). The noise profile seen for the DLRR is functionally identical. The nominal frequency distributions were constructed using a symbol rate $S = 100$ kHz.

same physical setup, differing only by the use of a second LO and an IF, we take $E_0(S)$ to be identical for both systems. Thus, the difference in EVM seen in figure (7) is entirely due to $E(S)$. We further assume that the non-atomic noise is primarily multiplicative, as residual $1/f$ laser intensity fluctuations are well known to affect the performance of Rydberg sensors [33]. In this situation, $E(S)$ results from complex valued noise described by

$$N(t) = N_M(t) + N_A(t) \approx N_M(t), \quad (\text{B2})$$

where the subscripts M and A are used to denote multiplicative and additive noise effects, respectively, and the real and imaginary parts of $N(t)$ refer to noise in I and Q , respectively. Since $N_M(t)$ scales with the amplitude of the received signal, $E(S)$ is expected to scale with the overlap of the non-atomic noise profile with the nominal signal distribution. The envelope of the frequency distribution of both the real

and imaginary components of the nominal signal expected from the DLRR is

$$FT[A(t, S)] = \tilde{A}(f, S) = \frac{S}{\pi f} \sin(\pi f/S), \quad (\text{B3})$$

where $FT[A(t, S)]$ is the Fourier transform of the nominal signal envelope, $A(t, S)$, with respect to time t . We also use $\omega = 2\pi f$ to express functions in the frequency domain using units Hz. Prior to mixing down to baseband, the envelope of the frequency distribution of the signal expected from the CRR is

$$\begin{aligned} \tilde{A}(f, S) &= \frac{S}{\pi(f-S)} \sin(\pi(f-S)/S) \\ &\pm \frac{S}{\pi(f+S)} \sin(\pi(f+S)/S), \end{aligned} \quad (\text{B4})$$

where the second term is positive for the real part and negative for the imaginary part. The real part of both envelopes are plotted in figure (10) against the noise profile with $S = 100$ kHz after truncation with the appropriate spectral brickwall filter. Using the convolution theorem, we cross-correlate the quantity $A(t, S)$ with the error $N(t)$ via multiplication in the Fourier domain:

$$\begin{aligned} FT[A(t, S) \star N(t)] &= FT[A^*(-t, S) * N(t)] \\ &= \tilde{A}^*(f, S) \tilde{N}(f), \end{aligned} \quad (\text{B5})$$

where \star denotes cross-correlation, $*$ denotes convolution, and $\tilde{N}(f)$ is the Fourier transform of $N(t)$. The absolute value of this quantity (i.e., $|\tilde{A}^*(f, S) \tilde{N}(f)|$) allows one to quantify the relative magnitude of multiplicative noise between measurements at a given frequency.

While this work calculated EVM by taking only the center point of each symbol's duration, one might more generally wish to average over some window of the symbol's duration centered on the symbol's midpoint [34]. To describe how multiplicative noise contributes to EVM, we more generally consider how averaging over this window alters the calculated EVM. The average noise over a window of the n^{th} sym-

bol's duration centered on the symbol's temporal midpoint is described by

$$\begin{aligned} N_n &= \frac{1}{T-\Delta} \int_{t_n-(T-\Delta)/2}^{t_n+(T-\Delta)/2} N(t) dt \\ &= \frac{1}{T-\Delta} \int_{-\infty}^{\infty} N(t) (H(t-t_n+(T-\Delta)/2) \\ &\quad - H(t-t_n-(T-\Delta)/2)) dt \\ &= \int_{-\infty}^{\infty} N(t) \Pi\left(\frac{t-t_n}{T-\Delta}\right) dt, \end{aligned} \quad (\text{B6})$$

where $H(t)$ is the Heaviside step function and we use $\Pi((t-t_n)/(T-\Delta))$ to denote a rectangular pulse of width $T-\Delta$ centered at t_n with a normalized area of one. Noting $\Pi((t-t_n)/(T-\Delta)) \in \mathbb{R}$, we may re-express our average as a cross-correlation evaluated at time t_n ,

$$N_n = \left[\Pi\left(\frac{t-t_n}{T-\Delta}\right) \star N(t) \right] \Big|_{t=t_n}. \quad (\text{B7})$$

The Fourier transform of $\Pi((t-t_n)/(T-\Delta))$ will incur a phase factor $\exp(i\omega t_n)$ resulting from the fact that the pulse is centered at t_n . We apply the convolution theorem again to express the frequency distribution of N_n as

$$\tilde{N}_n(f, S) = \tilde{\Pi}^*(f, S) \tilde{N}(f), \quad (\text{B8})$$

While $\tilde{N}_n(f, S)$ will be complex-valued, EVM is calculated via the magnitude of the error vector lying in the complex plane. With this in mind, we take the absolute value of $\tilde{N}_n(f)$ to retrieve the magnitude of noise at a given frequency. In doing so, we use $|\tilde{\Pi}^*(s, S)| = |\tilde{\Pi}(f, S)|$, rendering the phase factor $\exp(i\omega t_n)$ inconsequential. As a result, $|\tilde{\Pi}(f, S)|$ is equivalent to the magnitude of the Fourier transform of $\Pi(t/(T-\Delta))$, which we denote using $|\tilde{\Pi}_0(f, S)|$. Explicitly,

$$\tilde{\Pi}_0(f, S) = \frac{S}{\pi f(1-S\Delta)} \sin\left(\frac{\pi f(1-S\Delta)}{S}\right). \quad (\text{B9})$$

Using equations B5 and B8, we conclude that non-atomic EVM for the n^{th} symbol must scale with

$$E_n(S) \propto \int_{-\infty}^{\infty} \tilde{B}(S) |\tilde{A}^*(f, S) \tilde{\Pi}_0(f, S) \tilde{N}(f)| df, \quad (\text{B10})$$

where $\tilde{B}(S)$ refers to a spectral brickwall filter of width $2S$, centered on the peak of the central lobe of $\tilde{A}(f, S)$ (the positive frequency peak is used for heterodyne data). While the expression above is only for a single symbol, taking the magnitude of $\tilde{N}_n(f)$ has allowed us to ignore phase accumulation from t_n as we move from one symbol to the next. Thus, the expression for any symbol in the transmission is identical to the expression above, meaning it effectively provides the total non-atomic EVM, $E(S)$.

We use equation B10 to calculate the relative quantity of non-atomic, multiplicative noise present in the EVM results. Since we take only the center point of the symbol duration, we use this result in the limit that $\Delta \rightarrow T = 1/S$, meaning the factor $\tilde{\Pi}_0(f, S)$ reduces to one. Since the ratio of atomic noise to non-atomic noise is unknown, we scale all the calculated values of $E(S)$ by a fixed constant which minimizes

the difference in EVM between the datasets from each receiver, a choice motivated by the assumption that $E_0(S)$ is identical for both systems. Explicitly, figure (9b) plots the result of equation B10 for each measurement multiplied by this scalar value.

The fact that the removal of multiplicative pink noise yields a comparable EVM for both systems indicates that both the distribution (e.g., pink noise versus white noise) and type (additive versus multiplicative) directly influences which system may be more effective in demodulating a given signal. However, the fundamental limits of each system are still driven primarily by atomic noise, leaving open the possibility that an idealized DLRR could outperform its conventional counterpart. To realize such a receiver, $1/f$ laser intensity noise would need to be drastically reduced.

-
- [1] N. Schlossberger, N. Prajapati, S. Berweger, A. P. Rotunno, A. B. Artusio-Glimpse, M. T. Simons, A. A. Sheikh, E. B. Norrgard, S. P. Eckel, and C. L. Holloway, Rydberg states of alkali atoms in atomic vapour as si-traceable field probes and communications receivers, *Nat. Rev. Phys.* **6**, 606 (2024).
 - [2] C. T. Fancher, D. R. Scherer, M. C. S. John, and B. L. S. Marlow, Rydberg atom electric field sensors for communications and sensing, *IEEE Trans. Quantum Eng.* **2**, 1 (2021).
 - [3] C. S. Adams, J. D. Pritchard, and J. P. Shaffer, Rydberg atom quantum technologies, *IEEE Trans. Antennas Propag.* **53**, 012002 (2019).
 - [4] D. H. Meyer, K. C. Cox, F. K. Fatemi, and P. D. Kunz, Digital communication with rydberg atoms and amplitude-modulated microwave fields, *Appl. Phys. Lett.* **112** (2018).
 - [5] K. C. Cox, D. H. Meyer, F. K. Fatemi, and P. D. Kunz, Quantum-limited atomic receiver in the electrically small regime, *Phys. Rev. Lett.* **121**, 110502 (2018).
 - [6] Z. Song, H. Liu, X. Liu, W. Zhang, H. Zou, J. Zhang, and J. Qu, Rydberg-atom-based digital communication using a continuously tunable radio-frequency carrier, *Opt. Express* **27**, 8848 (2019).
 - [7] C. L. Holloway, M. T. Simons, A. H. Haddab, J. A. Gordon, and S. D. Voran, A multiple-band rydberg atom-based receiver: Am/fm stereo reception, *IEEE Antennas and Propagation Magazine* **63**, 63 (2021).
 - [8] J. S. Otto, M. K. Hunter, N. Kjærgaard, and A. B. Deb, Data capacity scaling of a distributed rydberg atomic receiver array, *J. Appl. Phys.* **129** (2021).
 - [9] X.-H. Liu, K.-Y. Liao, Z.-X. Zhang, H.-T. Tu, W. Bian, Z.-Q. Li, S.-Y. Zheng, H.-H. Li, W. Huang, H. Yan, *et al.*, Continuous-frequency microwave heterodyne detection in an atomic vapor cell, *Phys. Rev. Appl.* **18**, 054003 (2022).
 - [10] D. H. Meyer, J. C. Hill, P. D. Kunz, and K. C. Cox, Simultaneous multiband demodulation using a rydberg atomic sensor, *Phys. Rev. Appl.* **19**, 014025 (2023).
 - [11] J. Yuan, T. Jin, L. Xiao, S. Jia, and L. Wang, A rydberg atom-based receiver with amplitude modulation technique for the fifth-generation millimeter-wave wireless communication, *IEEE antennas and wireless propagation letters* **22**, 2580 (2023).
 - [12] Y. Cai, S. Shi, Y. Zhou, Y. Li, J. Yu, W. Li, and L. Li, High-sensitivity rydberg-atom-

- based phase-modulation receiver for frequency-division-multiplexing communication, *Phys. Rev. Appl.* **19**, 044079 (2023).
- [13] M. Schmidt, S. Bohaichuk, V. Venu, F. Christaller, C. Liu, F. Ripka, H. Kübler, and J. P. Shaffer, Rydberg-atom-based radio-frequency sensors: amplitude-regime sensing, *Opt. Express* **32**, 27768 (2024).
- [14] G. Gao, M. Chen, H. Feng, Z. Zhu, A. Chen, Z. Wu, T. Mao, W. Dai, P. Peng, and D. Zheng, Rydberg communication antennas with self-decoupling for dynamic radar interference based on heterodyne technology, *Appl. Phys. Lett.* **126** (2025).
- [15] M. T. Simons, A. H. Haddab, J. A. Gordon, and C. L. Holloway, A rydberg atom-based mixer: Measuring the phase of a radio frequency wave, *Appl. Phys. Lett.* **114** (2019).
- [16] M. Jing, Y. Hu, J. Ma, H. Zhang, L. Zhang, L. Xiao, and S. Jia, Atomic superheterodyne receiver based on microwave-dressed rydberg spectroscopy, *Nat. Phys.* **16**, 911 (2020).
- [17] K. Yang, R. Mao, Q. An, J. Li, Z. Sun, and Y. Fu, Amplitude-modulated rf field rydberg atomic sensor based on homodyne technique, *Sens. Actuators, A* **351**, 114167 (2023).
- [18] S. Berweger, A. B. Artusio-Glimpse, N. Prajapati, A. P. Rotunno, N. Schlossberger, D. Shylla, K. R. Moore, M. T. Simons, and C. L. Holloway, Independent rydberg atom sensing using a dual-ladder scheme, *Appl. Phys. Lett.* **124** (2024).
- [19] A. K. Robinson, N. Prajapati, D. Senic, M. T. Simons, and C. L. Holloway, Determining the angle-of-arrival of a radio-frequency source with a rydberg atom-based sensor, *Appl. Phys. Lett.* **118** (2021).
- [20] M. T. Simons, A. H. Haddab, J. A. Gordon, and C. L. Holloway, A rydberg atom-based mixer: Measuring the phase of a radio frequency wave, *Appl. Phys. Lett.* **114** (2019).
- [21] D. Manchiaiah, S. Oliver, S. Berweger, C. L. Holloway, and N. Prajapati, Probing bandwidth and sensitivity in rydberg atom sensing via optical homodyne and rf heterodyne detection, *Phys. Rev. A* **113**, 013729 (2026).
- [22] R. Finkelstein, S. Bali, O. Firstenberg, and I. Novikova, A practical guide to electromagnetically induced transparency in atomic vapor, *New J. Phys.* **25**, 035001 (2023).
- [23] K. DeRose, K. Jiang, J. Li, M. Julius, L. Zhuo, S. Wenner, and S. Bali, Producing slow light in warm alkali vapor using electromagnetically induced transparency, *Am. J. Phys.* **91**, 193 (2023).
- [24] N. Šibalić, J. D. Pritchard, C. S. Adams, and K. J. Weatherill, Arc: An open-source library for calculating properties of alkali rydberg atoms, *Comput. Phys. Commun.* **220**, 319 (2017).
- [25] R. A. Shafik, M. S. Rahman, A. R. Islam, and N. S. Ashraf, On the error vector magnitude as a performance metric and comparative analysis, in *2006 International Conference on Emerging Technologies (IEEE, 2006)* pp. 27–31.
- [26] M. A. Richards *et al.*, *Fundamentals of radar signal processing*, Vol. 1 (Mcgraw-hill New York, 2005).
- [27] Y.-T. Chan, J. Plews, and K. Ho, Symbol rate estimation by the wavelet transform, in *1997 IEEE International Symposium on Circuits and Systems (ISCAS)*, Vol. 1 (IEEE, 1997) pp. 177–180.
- [28] P. Ciblat, P. Loubaton, E. Serpedin, and G. B. Giannakis, Asymptotic analysis of blind cyclic correlation-based symbol-rate estimators, *IEEE Trans. Inf. Theory* **48**, 1922 (2002).
- [29] M. A. Elgenedy and A. Elezabi, Blind symbol rate estimation using autocorrelation and zero crossing detection, in *2013 IEEE International Conference on Communications (ICC)* (IEEE, 2013) pp. 4750–4755.
- [30] S. Majhi and T. S. Ho, Blind symbol-rate estimation and test bed implementation of linearly modulated signals, *IEEE Trans. Veh. Technol.* **64**, 954 (2014).
- [31] J. Kitching, Y. Shevy, J. Iannelli, and A. Yariv, Measurements of 1/f frequency noise reduction in semiconductor lasers using optical feedback with dispersive loss, *J. Light. Technol.* **11**, 1526 (1993).
- [32] S. M. Bohaichuk, D. Booth, K. Nickerson, H. Tai, and J. P. Shaffer, The origins of rydberg atom electrometer transient response and its impact on radio frequency pulse sensing, *Phys. Rev. Appl.* **18**, 034030 (2022).
- [33] Y. Tang, H. Zhou, C. Yang, S. Ren, S. Wang, and C. Lu, Noise performance of a rydberg atomic receiver, *Phys. Rev. A* **112**, 043106 (2025).
- [34] R. Sadr and W. Hurd, Detection of signals by the digital integrate-and-dump filter with off-set sampling, *Telecommun. Data Acquis. Rep.* (1987).